FISEVIER

Contents lists available at ScienceDirect

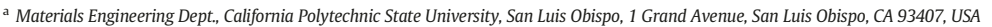
Materials and Design

journal homepage: www.elsevier.com/locate/matdes



Development of a gall-resistant stainless-steel hardfacing alloy

Ryan Smith ^a, Marc Doran ^b, David Gandy ^c, Suresh Babu ^d, Leonardo Wu ^e, Antonio J. Ramirez ^b, Peter M. Anderson ^{b,*}



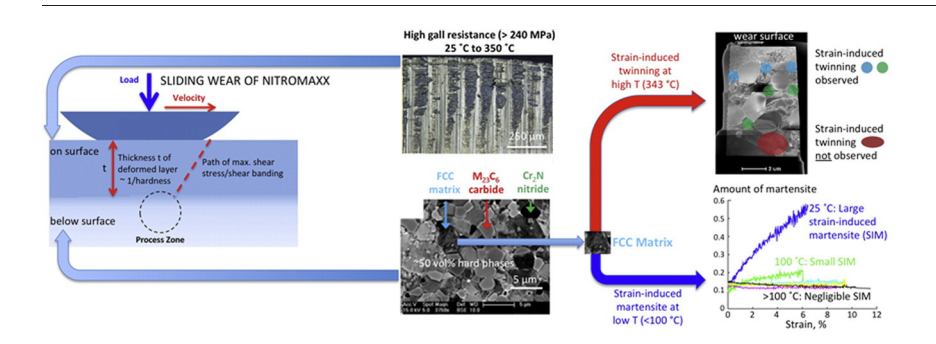
^b Dept. Materials Science and Engineering, The Ohio State University, 2041 N. College Rd., Columbus, OH 43210, USA

^e Brazilian Nanotechnology National Laboratory-LNNano, r 000, R. Giuseppe Máximo Scolfaro, Campinas, SP, Brazil



- A new wear/gall resistant stainless steel alloy is developed that rivals the performance of Stellite from T = 300 to 625 K;
- The alloy design strategy is to suppress strain localization hard phases and matrix strain hardening;
- This is achieved through powder metallurgy and annealing to achieve extraordinarily high nitrogen strengthening;
- An enhanced strain-induced martensite phase transformation at 298 K and twinning at 625 K are observed.

GRAPHICAL ABSTRACT



ARTICLE INFO

Article history: Received 3 September 2017 Received in revised form 9 January 2018 Accepted 10 January 2018 Available online 12 January 2018

Keywords: Wear Alloy design Stainless steel Phase transformation Twinning Stacking fault energy

ABSTRACT

This work details the development of a new cobalt-free stainless steel powder metallurgy hardfacing alloy designed to replace Stellite 6, a cobalt-based hardfacing alloy used in nuclear valve applications. The fundamental strategy centers on alloying stainless steels with up to 0.5 wt% nitrogen, which is shown to increase both the volume fraction of hard phase precipitates and the strain-hardening rate of the matrix. The resultant alloy, Nitromaxx, exhibits galling performance that is comparable to Stellite 6, up to 350 °C. This performance is attributed to the suppression of strain localization events associated with galling. In particular, transmission electron microscopy and diffraction measurements from tensile tests show that the nitrogen addition decreases the calculated matrix stacking fault energy and enhances both deformation-induced martensite transformation at room temperature and deformation twinning at elevated temperature. These strain-hardening mechanisms, coupled with the increase in precipitate volume fraction, effectively suppress localization and enhance galling resistance up to 350 °C. The enhanced galling resistance cannot be rationalized in terms of tensile stress-strain response alone.

© 2018 Elsevier Ltd. All rights reserved.

1. Introduction

Hardfacing alloys provide high tribological wear resistance under unlubricated sliding conditions. Such conditions are prevalent in power plant turbines, pumps, valve seats, and numerous other

* Corresponding author. E-mail address: anderson.1@osu.edu (P.M. Anderson). applications. Cobalt-based Stellite alloys have excellent resistance to galling, a severe form of adhesive wear that involves plastic flow or material transfer during metal-to-metal sliding under a nominal contact pressure [1]. They are often used in wear-resistant valve applications in power plants [2].

Despite a superior galling performance, Stellite 6 has a significant drawback: corrosion and wear debris can be activated to radioactive Co-60 and circulate through the nuclear core of a power plant. This

^c The Electric Power Research Institute, 1300 W WT Harris Blvd., Charlotte, NC 28262, USA

^d Dept. Mechanical, Aerospace, and Biomedical Engineering, University of Tennessee – Knoxville, 1512 Middle Dr., Knoxville, TN 37996, USA

radioactive isotope of Co is considered to be the largest contributor to occupational radiation exposure in nuclear power plants, resulting in a large incentive to replace Co-based hardfacing alloys with Co-free alternatives. Until now, a cobalt-free, gall-resistant, hardfacing alloy has not been available to address this problem.

This paper outlines the design approach, implementation, testing, microstructural characterization, and deformation mechanisms in Nitromaxx, a new Co-free hardfacing alloy with excellent gallresistance performance. Section 2 describes the basis for a key hypothesis that underlies this work; high galling resistance can be achieved by suppressing strain localization. Section 3 details the experimental approach to increase the nitrogen content in NOREM 02, a Co-free stainless steel alloy. Nitrogen is the target for compositional modification because at high concentrations in stainless steels, it has been observed to decrease the stacking fault energy [3-6]. This affects the planarity of slip [7], enhances the kinetics of a strain-induced martensitic transformation [8-11], and promotes deformation twinning at higher concentrations (e.g., 0.99 wt% N) [12]. Nitrogen can also increase the volume fraction of hard precipitates [13]. Martensite formation, twinning, and hard precipitates can help impart work hardening and suppress strain location [12, 14]. More recently, steels with higher nitrogen have been achieved using additive manufacturing methods, thus augmenting the strain-induced martensite transformation [15, 16]. The benefits of nitrogen addition in the resulting alloy, Nitromaxx, when tested from RT to 343 °C, are documented in Section 4. Nitrogen is shown to increase the volume fraction of hard phases and enhance a deformationinduced FCC-to-BCC martensite transformation at room temperature and twinning at elevated temperature (350 °C). The conclusions support the hypothesis that the superior gall resistance of Nitromaxx is coupled to microstructural features and deformation mechanisms that effectively suppress strain localization.

2. Design approach

This investigation builds on a fundamental observation in prior work [17] that the initiation of galling scars in stainless steels is associated with localized shear deformation under a sliding contact. Fig. 1a from that work shows physical evidence of shear localization in debris near a gall scar. The elongated shape and the sharp demarcation in the deformed, aligned microstructure from the relatively undeformed counterpart below provide evidence of strain localization.

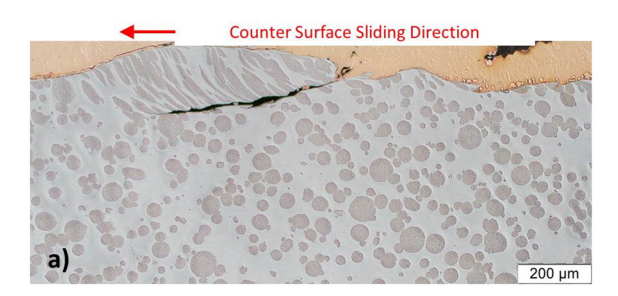
This observation motivated the hypothesis that galling in stainless steels can be reduced by the suppression of shear localization. This may not extend to other alloys in which the mechanism of severe adhesive differs. Fig. 1b outlines a two-part strategy to minimize localization. The first strategy is *geometric*: minimize the scale over which localization can occur by reducing the depth of the highly-deformed nanocrystalline layer in which localization events form. The second strategy is *constitutive*: impart plastic flow properties that suppress shear localization. The proposed approach to achieve the geometric strategy is to reduce asperity size and increase hardness. These actions are expected to

decrease the thickness of the highly deformed nanocrystalline layer [17] and reduce the scale of galling. The proposed approach to achieve the constitutive strategy is to incorporate hard secondary phases that are difficult to shear [18] and to promote large strain hardening of the matrix as to diffuse strain localization [19].

Fig. 2 shows a road map that details the mechanistic strategies in this work. The aforementioned fundamental hypothesis and strategies to suppress localization are detailed in the first and second columns. The third column lists specific microstructural modifications that include (1) increasing interstitial solution strengthening; (2) inducing plastic deformation mechanisms that increase matrix strain hardening; and (3) adding hard secondary phases. Interstitial solution strengthening is known to increase hardness in stainless steels [20], which is expected to decrease asperity size and reduce the thickness of the nanocrystalline layer. The increase in hardness aligns with the *geometric* strategy to decrease the scale of stress redistribution under the asperity. The reduced scale decreases the local driving force for adhesive wear processes [21–22], including simple adhesive wear and galling.

The third column also details the *constitutive* strategies to suppress shear localization. Strain hardening of the FCC matrix in stainless steels can be achieved by decreasing the stacking fault energy (SFE) [23]. A reduction in SFE is known to promote dissociation of perfect dislocations, thereby suppressing the ability of dislocations to circumvent obstacles via cross slip [24]. Dislocations are therefore more likely to be immobilized at defect intersections and produce Lomer-Cottrell locks and other reactions that pin dislocations [24]. A reduction in SFE can also aid deformation twinning, which introduces area defects (twins) that can act as barriers for increased strain hardening, as demonstrated in TWIP type steels [25, 26]. A reduced SFE can also aid the formation of defects that nucleate martensite [8, 27-29], a phase that can block dislocation motion and enhance strain hardening. Finally, hard second phases (e.g. carbides and nitrides) can inhibit shear band propagation and suppress large-scale strain-localization events. These trends follow from studies of metals [30] and cermet-type materials [31] on strainlocalization properties [32].

The last column of Fig. 2 proposes the addition of nitrogen to stainless steel to achieve all three microstructural modifications shown in column 3. First nitrogen additions can increase interstitial solution hardening in the FCC matrix. Second, studies [33–35] show that higher concentrations (>0.2 wt% N) can significantly decrease SFE and promote ε-martensite (HCP) formation [36] during straining at room temperature, although small additions to conventional SS grades are shown to do the opposite [20]. This non-monotonic effect may be due to segregation or clustering of nitrogen to stacking-faults [5] or to a constitutive thermodynamic interaction [37]. Successive decreases in SFE can augment the dominant inelastic deformation mechanism from: (1) dislocation cross-slip and forest hardening; to (2) planar slip from extended dislocations; to (3) deformation twinning; and finally to (4) straininduced martensite (FCC to HCP) [38]. The ability to invoke concurrent mechanisms has been used to explain the wear-rate dependence on stacking fault energy in several FCC materials [39]. Finally, super-



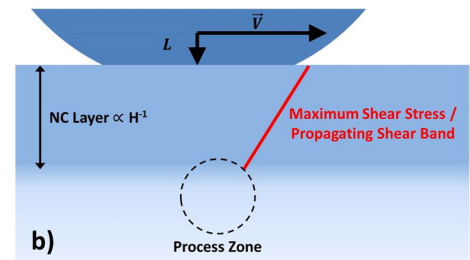


Fig. 1. (a) Cross-section view through a galling scar in a stainless steel with precipitates showing severe localization associated with scar and wear debris formation [3]; (b) Schematic depicting the development of a shear band through a highly deformed, nanocrystalline region with a thickness that scales with the average asperity size (inversely proportional to hardness, in the Archard wear regime).

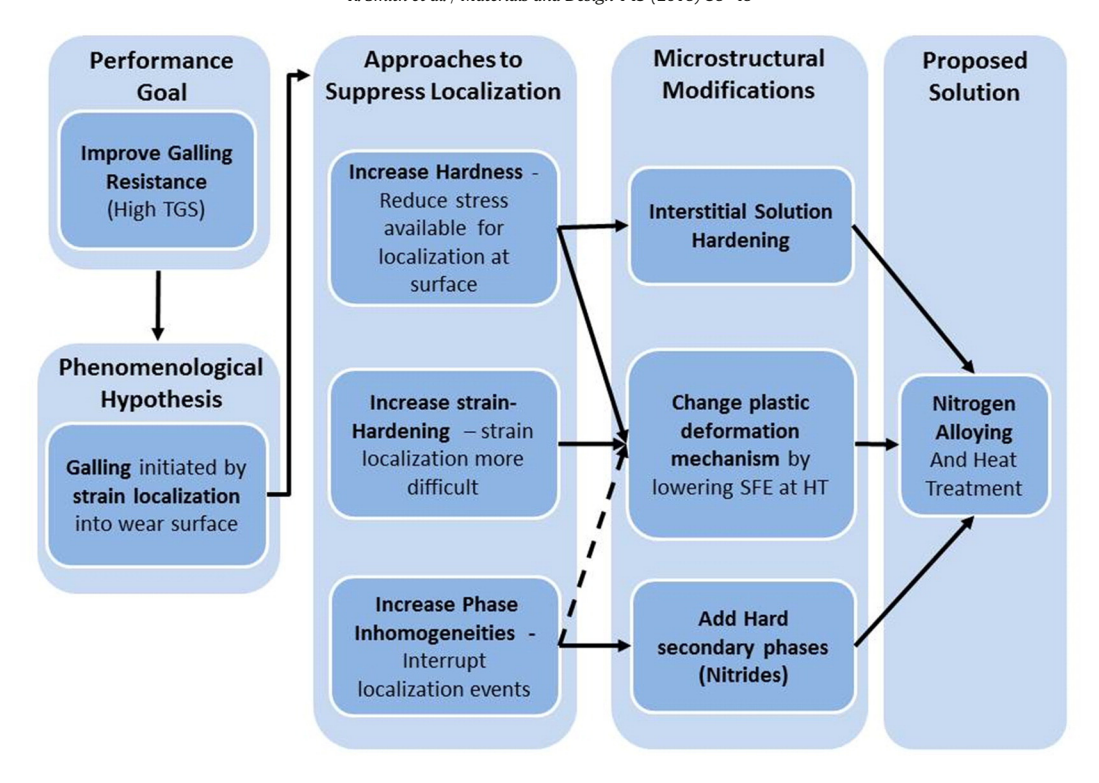


Fig. 2. Flow chart indicating the alloy design approach, from performance goals to a proposed solution involving nitrogen alloying and heat treatment. TGS = threshold galling stress; SFE = stacking fault energy; HT = high temperature (343 °C).

saturation of nitrogen will lead to nitride formation in stainless steels during high temperature processing. Nitride formation is associated with improved wear properties in a wide array of high-nitrogen stainless steels, such as 304LN and the Nitronic alloy series [1, 22, 40]. Large (>1 μm), hard particles in a metal matrix have been shown to suppress strain-localization and shear banding in a variety of cermet materials such as Al-SiC [32] and Co-WC composites. The present work pursues nitrogen additions up to 0.5 wt% N, compared to the 304LN and Nitronic alloy series that have 0.2 wt% nitrogen or less.

3. Experimental methods

Table 1 shows a series of hardfacing alloy compositions that were considered in this work. The composition for an existing reference alloy, NOREM 02, and the new alloy, Nitromaxx, are similar except that Nitromaxx is produced from powder with 0.51 wt% N vs. 0.17 wt% N for NOREM 02. Each alloy sample was prepared by sintering powder compacts at 1050 °C under vacuum for 10 h and then air cooling. A variety of normalizing/annealing heat treatments are also shown in Table 1. Each composition was then evaluated using galling tests, metallography, and electron microscopy.

ASTM G98 pin-on-block, self-mated gall tests were performed at room and elevated temperature (343 °C) to mimic conditions experienced by valves in pressurized water reactor conditions. Cylindrical specimens with mating surfaces were rotated relative to one another by 360°, using progressively larger normal (compressive) loads from one test to the next. The TGS was recorded as the nominal compressive stress at which pronounced grooving and metal transfer were observed, based on laser profilometry and optical microscopy as specified in the ASTM method. The threshold for galling and subsequent seizure was the primary performance parameter of interest and, for that reason, the ASTM G98 galling test was used exclusively to assess performance.

Microstructures were investigated using conventional metallography, X-ray diffraction (Rigaku SmartLab), and scanning electron microscopy (SEM-FEI ESEM XL-30). Powder metallurgy samples of increasing nitrogen content for the Nitromaxx alloy were prepared using Vilella's reagent

followed by electro-etching in boiling NaOH to reveal grain boundaries, carbides, and nitrides. Phase balance and identification were determined using a combination of X-ray diffraction quantification and point counting analysis from SEM micrographs. Simulations of the equilibrium structure were also performed using ThermoCalc (v6.2, TCFE4 database).

A methodology for microscopy and metallographic examination to protect wear surface features and debris was developed. Cross-sectional specimens normal to the wear surface were prepared by electroplating the wear surface with copper, followed by light polishing tangent to the gall sliding direction. Samples that were tested at or near the TGS were examined using scanning electron microscopy (SEM), energy dispersive spectroscopy (EDS), and electron back-scattered diffraction (EBSD) to determine the phases, structure, and microstructure near the wear surface (FEI ESEM XL-30). TEM analysis of the microstructure under the worn surface was performed on electron-transparent foils prepared by focus ion beam machining (FIB) in a Phillips model CM200 (accelerating voltage 200 KV).

The strain-induced martensite transformation was also investigated with respect to strain-evolution and temperature stability using in-situ X-ray diffraction (XRD). The in-situ XRD experiments were performed at the Nanotechnology Laboratory (LNNano) in Campinas, Brazil. A Gleeble thermomechanical simulator was set up in the path of a synchrotron X-ray beam at the beamline. An X-ray beam energy of 12 KeV (wavelength 1.033 Å) was used in a reflection geometry inside the experimental chamber. Information about the structure and fraction of various phases was collected during isothermal tensile testing at several temperatures under vacuum. Details of the experimental apparatus are available at http://lnnano.cnpem.br/laboratories/cpm/facilities/xtms/

4. Results

4.1. Galling properties

Table 2 shows that the Nitromaxx alloy has excellent room (RT) and high temperature (343 $^{\circ}$ C) galling behavior, comparable to or better than Stellite 6. In contrast, stainless steel 316 L displays poor performance

Table 1
Compositions (wt%) of the Melt and Annealing Temperature Used to Make Powder-Based Hardfacing Alloys, measured by electron-probe microanalysis (EPMA).

Alloy	Cr	Ni	Mn	Mo	Co	Si	W	С	N	Fe	Annealing T
Stellite 6	30	3	1	1.5	58	1.5	4	1			1325 K (1050 °C)
NOREM 02/1050	25	4	4	2	< 0.06	3.5		1.2	0.17	Bal.	1325 K (1050 °C)
NitroMaxx/1100	28	4	4	2		3.5		1.2	0.51 ^a	Bal.	1375 K (1100 °C) ^b

^a 0.30 and 0.44 Wt% N also studied.

at both temperatures and NOREM 02 shows excellent performance only at RT. Fig. 3 shows optical micrographs of NOREM 02, Nitromaxx, and Stellite 6 samples after high temperature G98 testing at 100 MPa. Both Nitromaxx (Fig. 3b) and Stellite 6 (Fig. 3c) show modest surface deformation with small (<50 µm) features, characteristic of excellent gall resistance. However, NOREM 02 (Fig. 1a) displays obvious signs of galling. This marked degradation in the NOREM 02 performance at high temperature is consistent with previous experimental studies [41]. The transition from excellent gall resistance at room temperature to poor resistance at elevated temperature has been correlated to the cessation of a strain-induced martensite transformation above 200 °C [42].

4.2. Surface oxides

Fig. 4 shows surface oxides (dark regions, top of images) on the Nitromaxx and Stellite 6 surfaces after elevated temperature G98 testing. These features are not present on surfaces with poor galling resistance (e.g., NOREM 02 at elevated temperature). They are indicative of localized, high temperatures near asperities during G98 wear tests. The localized high temperatures are hypothesized to increase with increasing hardness for a given nominal stress and coefficient of friction because a comparable nominal work rate is distributed over smaller asperities and thinner nanocrystalline regions (Fig. 1b) [2].

The 3–5 μm thick oxide layers in self-mated G98 tests of an austenitic stainless steel hardfacing alloy are similar to those in Stellite [43] and are usually indicative of good wear/galling properties. The layers are surface-adherent and have a lower effective atomic density, based on the reduced intensity in electron-backscattered images. They also show no contrast or coherent electron-backscatter diffraction and are not detected even in long exposure X-ray diffraction. This indicates that the structure is either amorphous or very highly faulted.

The mechanism of oxide formation is not certain because of the lack of in-situ tribological characterization. It may occur by re-deposition and mixing of debris [43] or by enhanced surface diffusion, yielding a layer that is thicker than that predicted from steady-state oxide kinetics [2]. The beneficial effects of this local oxidative behavior are hypothesized to be similar to those for (uniform) oxidative wear behavior. They include prevention of metal-to-metal surface contact and preferential deformation of the softer oxide layer. The result is a solid-phase lubricant-like effect with demonstrably beneficial wear properties.

4.3. Microstructure

Fig. 5 contrasts the microstructures of Stellite 6, NOREM 02, and Nitromaxx. Table 3 shows the volume fraction of phases in each alloy

Table 2ASTM G98 Threshold Galling Stress (MPa).

	Threshold Galling Stress (MPa)			
Alloy	298 K (25 °C)	625 K (343 °C)		
Stellite 6	>240	200		
NOREM 02/1050	>240	70		
Nitromaxx/1100	>240	>240		
Stainless Steel 316 L	1	0.1		

as determined from integrated peak intensities of X-ray diffraction data. These values were also substantiated through point counting methods in micrographs as in Fig. 5. All three alloys share the same feature that a FCC matrix is reinforced with $M_{23}C_6$ carbides. For Stellite 6 and NOREM 02, the relative fractions of matrix and carbides is similar. However, Nitromaxx has 15 vol% nitrides (Cr_2N) in addition to the carbides. Thus, it has a greater overall volume fraction of hard phases, which may serve to suppress shear localization. Nitromaxx also has a finer microstructure than NOREM 02 (compare Fig. 5b–c).

Fig. 6 shows that increasing wt% N in the melt during powder processing increases the volume fraction of nitride precipitates in a monotonic fashion. This trend is also supported by thermodynamic modeling of Nitromaxx using ThermoCalc software [32]. In particular, Fig. 7 shows output from ThermoCalc software for the Nitromaxx composition (wt% N = 0.51, Table 1). The molar fractions of nitrides and carbides are relatively constant over the temperature range 1050 to 1200 °C varying from 0.17 to 0.20 for $\rm M_{23}C_6$ and from 0.05 to 0.07 for $\rm Cr_2N$. A key consequence is that the equilibrium volume fraction of hard phases increases modestly with annealing temperature.

4.4. Matrix lattice parameter and composition

Fig. 8a shows that the lattice parameter of the FCC matrix, measured at room temperature by X-ray diffraction, monotonically increases with annealing temperature in the range of 1050 to 1200 °C for a 2-hour anneal. This is significant because the FCC matrix lattice parameter increases with interstitial (nitrogen and carbon) content [45]. Table 4 shows that both NOREM 02 and Nitromaxx samples have the same lattice parameter (3.585 \pm 0.005 Å) when sintered under pressure at 1000 °C, cooled, annealed at 1050 °C for 2 h, and then water quenched. The data therefore suggest a similar interstitial matrix composition in both Nitromaxx/1050 and NOREM02/1050, where the nomenclature / 1050 specifies the annealing temperature in °C. This is peculiar since the wt% N in the melt during powder processing was different for these alloys (Nitromaxx = 0.45 wt% N, NOREM 02 = 0.12 wt% N). When the annealing temperature was increased from 1050 to 1100 °C, the tabular results show that the matrix lattice parameter in Nitromaxx increased by ~0.5%.

Fig. 8b shows predictions from CALPHAD thermodynamic simulations that the mass% N in the FCC phase of Nitromaxx monotonically increases with annealing temperature. This is consistent with the experimentally observed increase in FCC phase lattice parameter with annealing temperature. The simulations also suggest that this trend extends to even greater annealing temperature, consistent with other work on similar stainless steel compositions [46]. The complex equilibria between the carbide and nitride species (Fig. 7) are a possible source of this nitrogen supersaturation. Small amounts of nitrogen can increase the lattice parameter (approximately 0.0009 Å per at% N [46]) and provide significant increases in yield strength (up to 120 MPa per wt% N) and strain hardening [47]. It is thus advantageous to increase the annealing temperature to increase interstitial content in the FCC matrix. However, constraints can intervene: if Nitromaxx is used as a hardfacing material on 316 L, the annealing temperature will be limited to 1100 °C (2 h), the maximum allowable ASTM annealing temperature for 316 L [46].

^b 1050, 1150, and 1200 °C also studied.

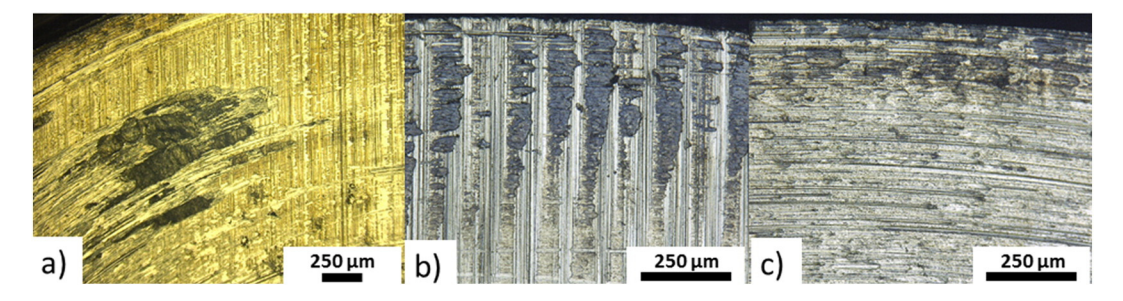


Fig. 3. Surfaces of: (a) NOREM02; (b) Nitromaxx; and (c) Stellite 6; after ASTM G98 testing at elevated temperature (350 °C) and 15 ksi (100 MPa) nominal compressive stress. The mm-scale galling scars in (a) contrast with the small (<50 μm) wear features in the Nitromaxx alloy and Stellite 6. The prominent vertical features in (a) and (b) and horizontal ones in (c) are from the ground surfaces before testing.

4.5. Uniaxial response and strain-induced martensite

Fig. 9 shows the results of in-situ X-ray diffraction during tensile testing of Nitromaxx at room temperature. In particular, straining at a rate of 0.01/s diminishes the volume fraction of the FCC matrix and increases that of the BCC martensite phase. Specifically, the FCC (111) and (200) peaks diminish from a large initial intensity (red) to a smaller intensity (green), while the BCC (220) peak increases in intensity from green to red (Fig. 9). Thus, a FCC-to-BCC strain-induced martensitic (SIM) transformation is observed. The changes in diffraction intensity with strain were quantified by fitting and normalizing the peaks, using a custom algorithm in the IgorPro and Matlab programming suites. The normalized intensities of the (111) and (110) peaks were used to determine the fraction of FCC and BCC phases in the matrix as a function of strain. The experimental set-up and data reduction method are detailed in Smith et al. [40].

Fig. 10 shows that the fraction of strain-induced martensite (SIM) evolves similarly with strain for both NOREM 02/1050 and Nitromaxx/1050. The similar SIM response prevails even though the alloys have a different %N melt composition (0.12 vs. 0.45) during processing and a different %vol. fraction of hard phases (0.33 vs. 0.44). However, both alloys have the same annealing temperature (1050 °C) and similar FCC matrix lattice parameter. This suggests that the evolution of SIM is controlled by %N in the matrix rather than the alloy composition.

Nitromaxx/1100 displays an increased SIM relative to Nitromaxx/1050. This is consistent with the results in Fig. 8 and Table 4 that a larger annealing temperature produces an increase in the FCC matrix lattice parameter and thus an increase in %N in the matrix. The larger %N is then hypothesized to lower the stacking fault energy in the matrix and increase the rate of SIM transformation via the formation of high-energy nucleation sites at shear band locations, as described in the Olson-Cohen model [8]. This is evidenced by the increased rate of martensite formation

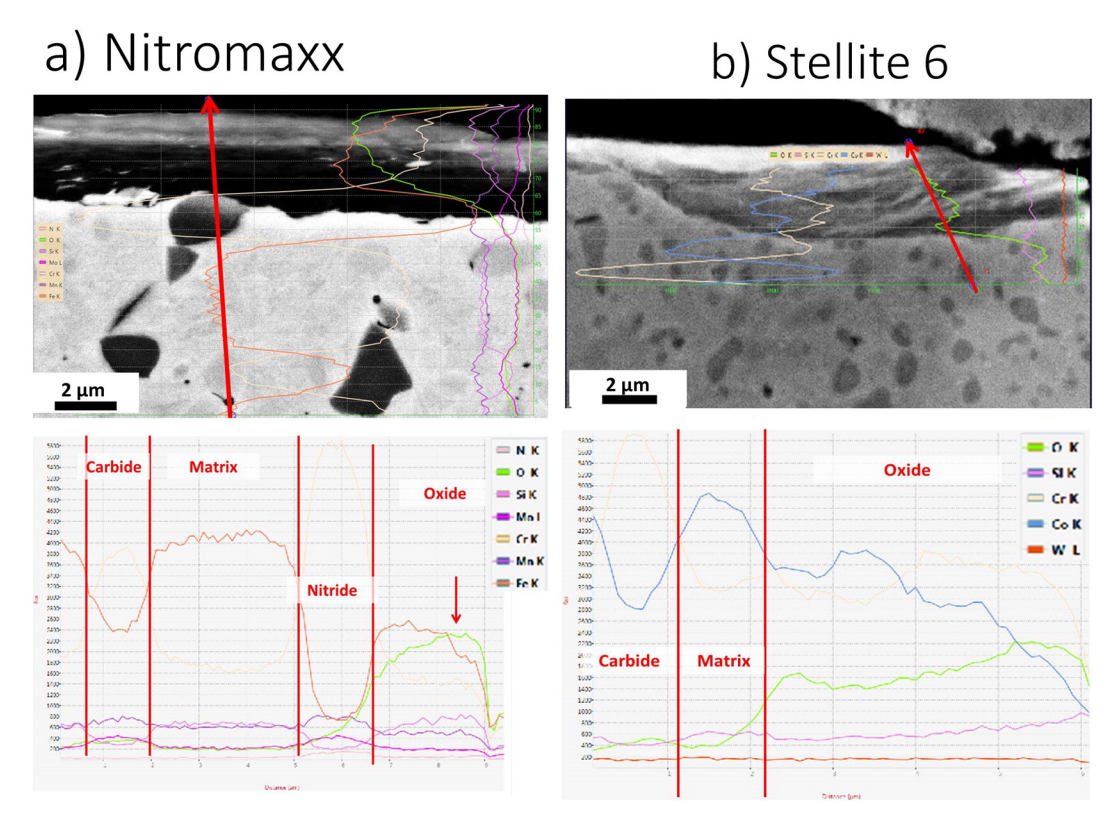


Fig. 4. Analysis of (a) Nitromaxx and (b) Stellite 6 samples after ASTM G98 testing at elevated temperature (343 °C) under a nominal compressive stress of 100 MPa. Upper images show sample cross-sections near the worn surface (top) using backscattered electron scanning electron microscopy. Arrows point to an oxide phase on the surface. Lower plots show chemical compositions based on EDS (XPS) measurements, indicating an elevated oxygen content near the surface.

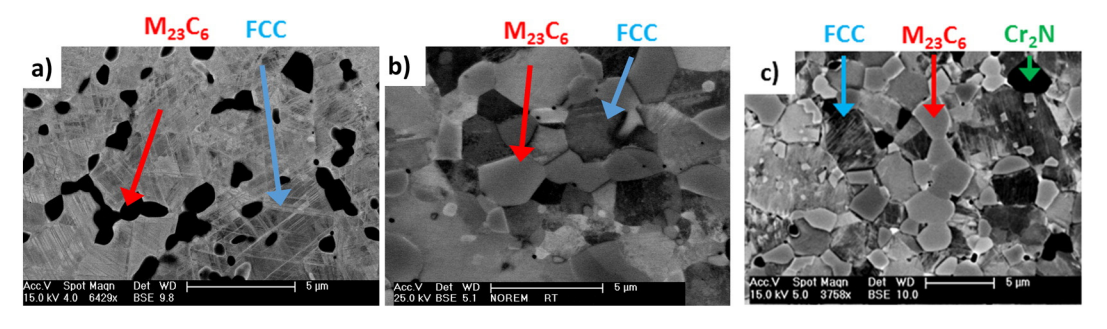


Fig. 5. Scanning electron microscope images showing the multiphase microstructure of (a) Stellite 6, (b) NOREM 02/1050, and (c) Nitromaxx/1100 as listed in Table 1. Note that the contrast of a particular phase (e.g., $M_{23}C_6$) can differ between micrographs due to relative differences in Z-number and crystal orientation.

Table 3Phase balance of hardfacing alloys, as determined from integrated peak intensities of X-ray diffraction data.

	Matrix	% Vol. Fraction	Secondary Phases	% Vol. Fraction
Stellite 6 NOREM 02/1050	FCC FCC	70 ± 10 65 + 5	M ₂₃ C ₆ M ₂₃ C ₆	30 ± 10 35 + 5
Nitromaxx/1100	FCC	50 ± 5	$M_{23}C_6$ $M_{23}C_6/Cr_2N$	35 ± 5 $35/15 \pm 5$

with strain and also the increased amount of martensite at the beginning of the test. The results can be fit to the Olson-Cohen [8] and other models [48, 11] for the SIM as a function of strain (see solid curves, Fig. 10). The data in Table 4 show that an increase in matrix lattice parameter is readily achieved by increasing the annealing temperature from 1050 to 1100 °C (compare Nitromaxx/1050 and Nitromaxx/1100, Table 4). However, an increase in %N in the melt without an increase in annealing temperature does not change the matrix lattice parameter (compare NOREM 02/1050, Nitromaxx/1050, Table 4). Thus, an increase in annealing temperature is observed to increase %N in the matrix (Fig. 8 and Table 4) and increase the strain-induced transformation rate (Fig. 10).

Fig. 11(a, b) show the uniaxial response and SIM, respectively, for NOREM 02/1050 and (c,d) show the respective data for Nitromaxx/1100, measured at different test temperatures. When the test temperature is increased from 23 to 150 °C, both alloys exhibit a decrease in strength. When the test temperature is increased further from 150 to 350 °C, the strength of NOREM 02/1050 continues to decrease but the strength of Nitromaxx/1100 remains relatively constant. The decrease in strength in the lower temperature range (23 to 150 °C) for both alloys can be rationalized in terms of the concomitant decrease in SIM shown in Fig. 11c–d.

However, the divergent trends in strength in the higher temperature range (150 to 350 °C) are not easily rationalized because both alloys suffer a comparable monotonic reduction in SIM with increasing test temperature. For example, the equivalent Md $_{50}$ (the temperature at which the matrix is 50 vol% martensite at 30% strain) is only 15 °C larger for Nitromaxx/1100 compared to NOREM 02/1050. The results also suggest that it is difficult to directly correlate uniaxial response and galling resistance. In particular, Stellite reaches 1200 MPa at 7% strain and is relatively insensitive to temperature from RT to 350 °C [42]. Thus, Stellite is considerably stronger than Nitromaxx at elevated temperature yet Table 2 shows Nitromaxx has comparable or better threshold galling resistance.

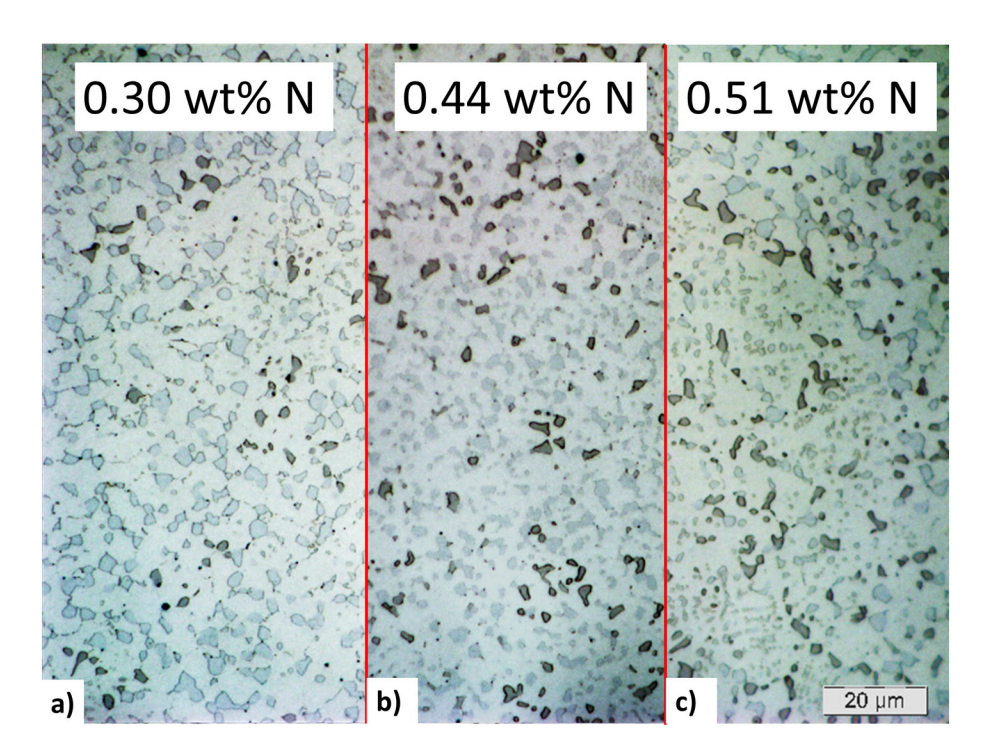


Fig. 6. Optical micrographs of alloys achieved by powder processing with (a) 0.30, (b) 0.44, and (c) 0.51 wt% N in the melt. Carbides are light blue/gray and nitrides are black. The alloy labeled c) is Nitromaxx as defined in Table 1. Samples were etched with Vilella's etchant and then boiled in NH_4OH .

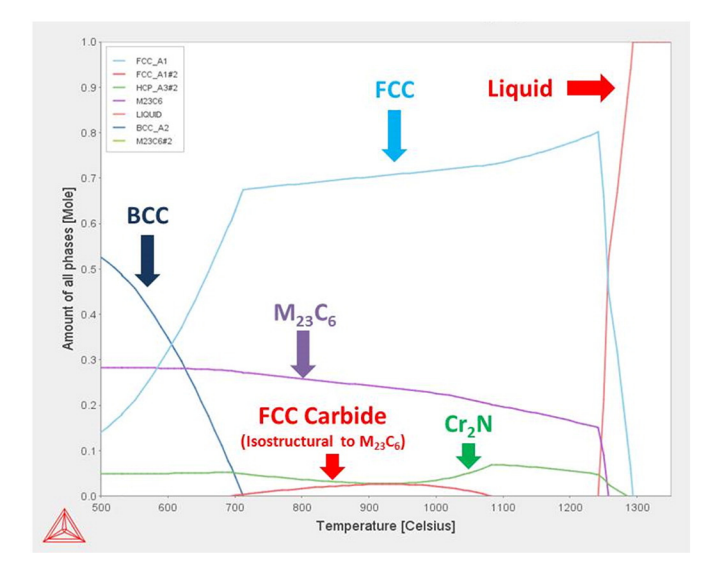


Fig. 7. Prediction of the equilibrium molar fraction of phases in Nitromaxx as a function of temperature, using ThermoCalc software [44]. The FCC matrix is in equilibrium with carbide and nitride phases and is meta-stable at low temperature.

4.6. Deformation twinning at elevated temperature (343 °C)

Fig. 12 is a transmission electron microscopy (TEM) image of a crosssection near the worn surface of a Nitromaxx/1100 sample, after G98 testing at 343 °C. This sample was prepared by coating the cut surface with Pt and the worn surface with Cu. then using focused ion beam (FIB) milling to trench, undercut, and thin it for TEM. Fine (<50 nm diameter) grains are observed within 2 µm of the wear surface (top); the severe deformation in this region obscures the ability to discern any twinning. However, twin laths are apparent in the six smaller circular regions located within 2 to 5 µm from the worn surface. No laths were observed in the larger elliptical region located >5 µm from the worn surface. Foils taken from outside the wear region confirm that the observed twining was due solely to the mechanical deformation of the material during the ASTM G98 galling test; it was not a pre-existing artifact of machining or sample preparation. TEM samples harvested from the opposing (block) surface from the same Nitromaxx/1100 G98 test have the same features. In contrast, foils taken from galled surfaces of NOREM 02/1050 samples revealed no deformation twinning. Thus, during G98 testing at 343 °C, deformation twinning occurred in Nitromaxx/1100 but not NOREM 02/1050. This motivates a hypothesis that the divergent trends in elevated temperature strength (Fig. 11a, b) and gall resistance (Table 2) are related to presence of deformation twinning in Nitromaxx/1100 and absence of it in NOREM 02/ 1050. At 350 °C, the tensile stress-strain response of NOREM 02/1050

Table 4Matrix Lattice Parameter, Melt Composition, and Hard Phase Fraction of Hardfacing Alloys.

ing T Lattice Parameter (Å)	,	Hard Phase Fraction (% Vol.)
1050) 3.582	0.12 0.45	33 ± 5 48 ± 5 44 + 5
	1050) 3.585	1050) 3.585 0.12 1050) 3.582 0.45

and Nitromaxx/1100 are quite comparable and far below the 1200 MPa strength reached by Stellite. The results suggest that twinning decreases the dependence of strength on temperature at elevated temperature. Also, the observed deformation twinning (Fig. 12) plus the larger hard phase volume fraction (Table 4) in Nitromaxx/1100 does not produce significantly larger tensile stress–strain response relative to NOREM 02/1050. These results underscore that the different threshold galling behaviors (Table 2) cannot be rationalized in terms of tensile stress–strain behavior.

Fig. 13a shows a higher resolution TEM image representative of the interior of the six smaller circles in Fig. 12. Fine, I nm-thick laths extend over several hundred nm and they intersect a hard phase in the upper left corner. Fig. 13b shows a selected-area diffraction pattern (SADP), typical of the three circular regions located 3 to 5 µm below the worn surface, where the grain size is large enough to obtain a pattern. The pattern confirms a clear twinning orientation along the (110) zone axis, consistent with deformation twins. Specifically, the diffraction pattern shows doubling of general diffraction spots, except those of type (*hhh*). These peaks correspond to a twin invariant plane of (111), the expected invariant plane in FCC phases present in stainless steels [49].

4.7. Reduced stacking fault energy

The effect of nitrogen on stacking fault energy (SFE) in the FCC matrix was considered to rationalize the observations of enhanced strain-induced martensite (SIM) at room temperature and deformation twinning at elevated temperature (343 °C) in Nitromaxx. A decrease in SFE has been proposed to affect SIM, by increasing both the thermodynamic driving force to form martensite as well as the density of nucleation sites for SIM [8]. The nucleation sites include intersections of stacking faults and twins, which can be promoted by a decrease in SFE. Although prior work has documented an enhanced FCC-to-BCC SIM and increased strain hardening when twinning accompanies SIM [41], the twinning observed in Nitromaxx/1100 does not appear to enhance SIM, relative to NOREM 02/1050 (Fig. 11b, d).

The stacking fault energy can be determined by measuring the equilibrium distance $d_{\rm eff}$ between partial dislocations in the FCC matrix. A governing equation based on dislocation theory [24] (see Eq. (10.14)),

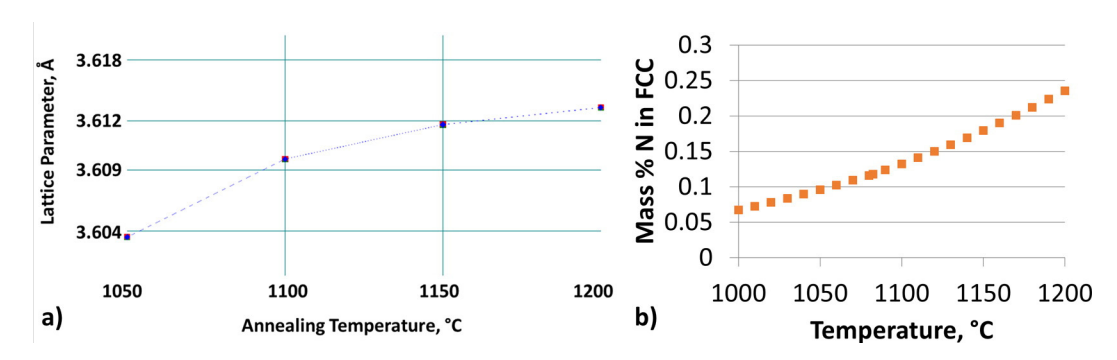


Fig. 8. (a) Lattice parameter of the FCC phase in Nitromaxx as a function of annealing temperature, as determined by X-ray diffraction. The Nitromaxx samples were heat treated at temperature for 2 h and water quenched. (b) Interstitial nitrogen in the FCC phase as a function of equilibrium temperature, as predicted from thermodynamic simulations (CALPHAD). ThermoCalc ® software [44] was used with suppression of the non-observed phase M₇C₃.

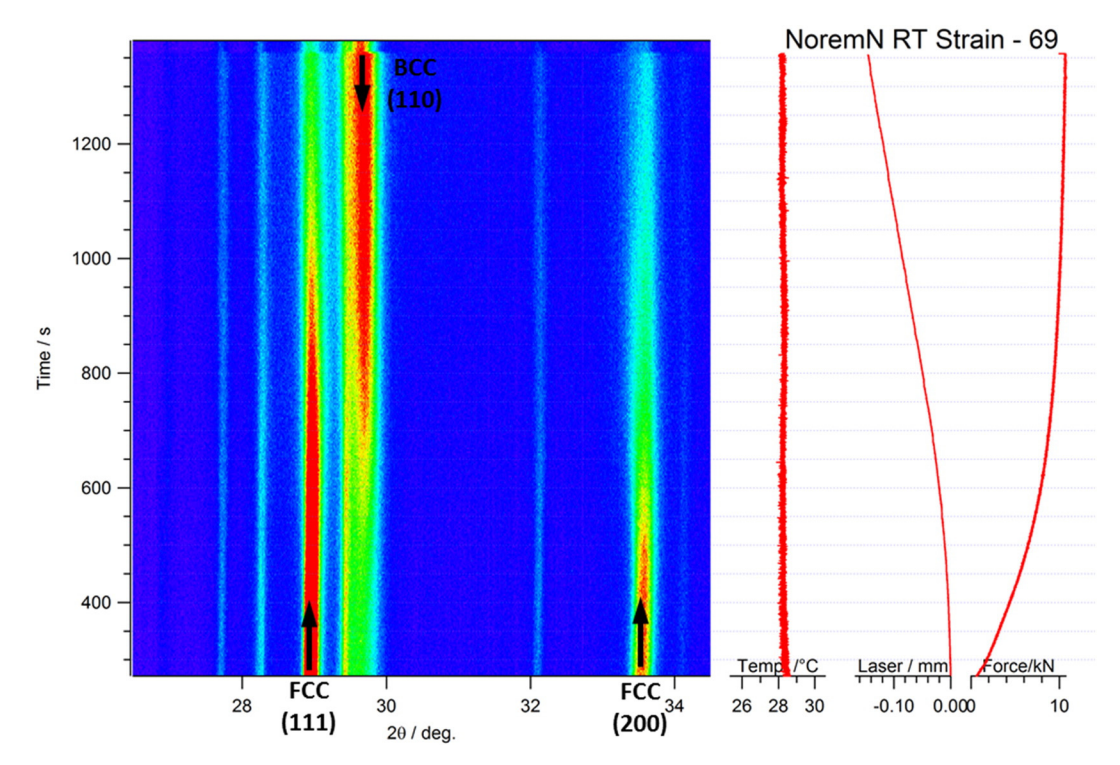


Fig. 9. Results from in-situ X-ray diffraction experiments during tensile testing of Nitromaxx at room temperature and a nominal strain rate of 0.01/s, showing diffraction patterns, test temperature (°C), change in cross-sectional dimension (mm, using laser extensometry), and tensile force (kN).

as applied by Aerts et al. [50] to anisotropic FCC crystals, is

$$\textit{SFE} = \frac{\mu_{\text{eff}}b^2}{8\pi d_{\text{eff}}} \frac{2 - \nu_{\text{eff}}}{1 - \nu_{\text{eff}}} \left(1 - \frac{2\nu_{\text{eff}}\,\cos\!2\beta}{2 - \nu_{\text{eff}}}\right) \tag{1}$$

Here, $b=a/6\langle 112\rangle$ is the magnitude of the Burgers vector of a partial dislocation in FCC stainless steel, for which a=3.608 Å is the lattice parameter, β is the angle between the Burgers vector and line direction of the perfect dislocation, and $\mu_{\rm eff}=73$ GPa and $\nu_{\rm eff}=0.31$ are the effective elastic shear modulus and Poisson's ratio, respectively, oriented along (111) slip planes that contain stacking faults. The effective numerical values have been shown to be an excellent fit to experimental data

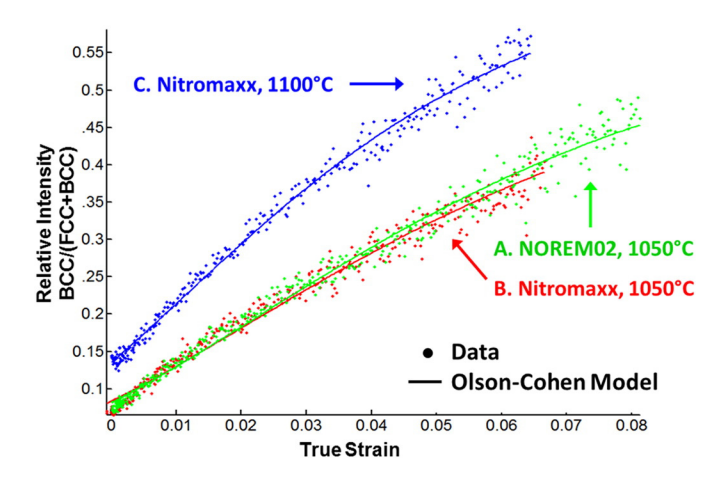


Fig. 10. Calculated fraction of BCC phase (martensite) as a function of tensile strain for the RT experiments described in Fig. 9, for NOREM 02/1050, Nitromaxx/1050, and Nitromaxx/1100 as defined in Table 4, where the nomenclature /1050 and /1100 specifies the annealing temperature in °C. The results for NOREM 02/1050 and Nitromaxx/1050 overlap whereas that for Nitromaxx/1100 is shifted up. The /1050 vs. /1100 nomenclature indicates a 1050 °C vs. 1100 °C anneal. The solid lines are a best fit to the Olson-Cohen model for SIM [8].

for FCC stainless steels [51]. An upper estimate to SFE values is obtained by setting $\beta = 90^{\circ}$, consistent with an edge dislocation. This upper bound was used because variations in strain and sample thickness prevented an accurate determination of β .

Fig. 14 shows TEM images from Nitromaxx/1100 and NOREM 02/1050 samples after G98 testing at 343 °C. A near [111] zone axis tilt was used to observe dislocation pairs on (111) slip planes (typical of FCC materials), using a $\langle -220 \rangle$ type diffraction vector. Following the approach of Pierce et al. [52], a g(4 g) diffraction condition was adopted for partial dislocation imaging, using an *inside out* diffraction condition reversal to determine the position of the partial dislocations that bound a stacking fault. Approximately 20–25 pairs of partial dislocations were imaged in each sample.

Table 5 shows that Nitromaxx/1100 has a larger d_{eff} and therefore smaller stacking fault energy (SFE) than NOREM 02/1050. In particular, the SFE of Nitromaxx is estimated to be <20 mJ/m², the empirical range below which twinning becomes accessible in FCC alloys [41, 6]. Thus, there is direct evidence that an increase in nitrogen from ~0.17 to ~0.5 wt% N, coupled with an increase in annealing temperature from 1050 °C to 1100 °C, decreases the SFE in the FCC matrix. There are three caveats to this observation. First, the assumption of $\beta = 90^{\circ}$ in Eq. (1) provides an upper bound to SFE values. Second, these values may not reflect those at 343 °C because the samples were imaged at RT following deformation at 343 °C. Third, the observed partial dislocations are unlikely to be in equilibrium due to internal stress from nearby defects, free surfaces, sample bending, and lattice resistance to dislocation motion. On average, the effects of internal stress should produce deviations that are centered about the equilibrium value because in principle, the internal stress in an unloaded sample should fluctuate around zero. Although these caveats are expected to affect the absolute values of SFE in each alloy, the difference in average stacking fault width supports the conclusion that Nitromaxx has a relatively smaller SFE.

5. Conclusions

A new gall-resistant stainless steel alloy, Nitromaxx, has been developed that rivals the room and elevated (343 °C) temperature threshold

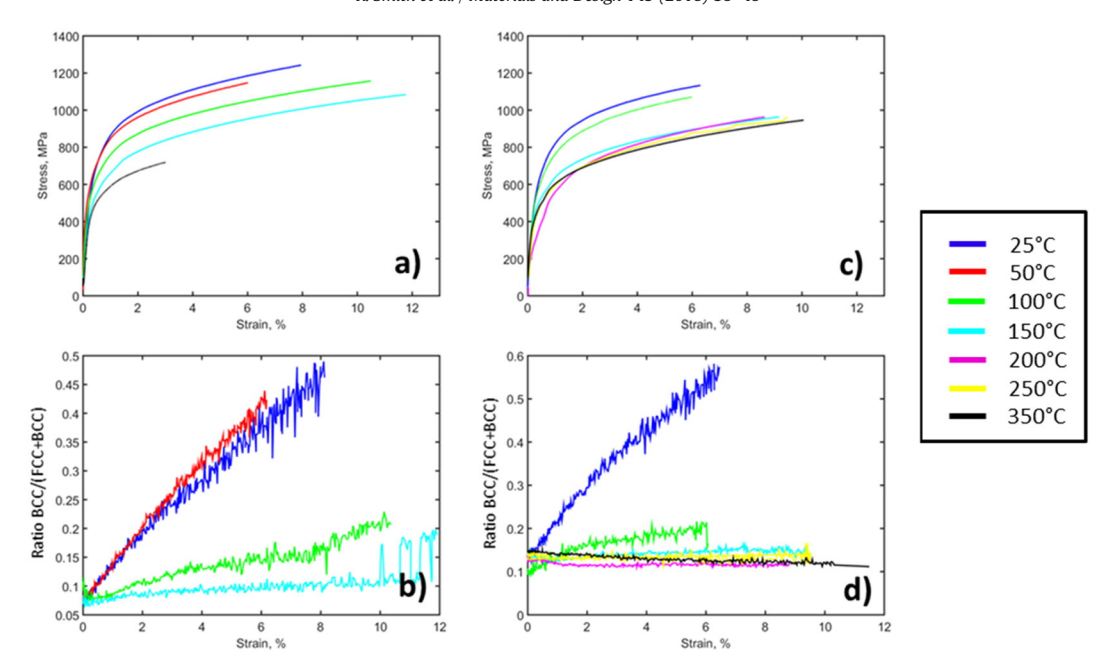


Fig. 11. Results from in-situ X-ray diffraction experiments during tensile testing at various temperatures, showing (a) stress-strain response and (b) calculated fraction of BCC phase for NOREM 02/1050 and corresponding results (c, d) for Nitromaxx/1100. Results for some temperatures (e.g., 350 °C in (b) and 50 °C in (d) are not available), yet the trends are apparent.

galling stresses of Stellite 6, a Co-base hardfacing alloy used in nuclear power plants. A benefit to Nitromaxx is that wear debris do not impose a radiation occupational health hazard as with Co-base alloys. The underlying approach for Nitromaxx was to modify a reference stainless steel alloy, NOREM02, so that strain localization is suppressed. The key strategies to suppress localization were to: (1) increase the volume fraction of hard phase particles, which can serve to arrest shear localization; (2) increase matrix flow strength, which can reduce plastic asperity sizes and dimensions of localization events; and (3) increase matrix strain hardening, which can serve to diffuse localized strain. These

strategies were achieved by a powder processing method, in which the nitrogen of the melt used to produce the powder was increased from ~0.17 to 0.5 wt%. The powder was then processed under hot isostatic pressure at 1050 °C and subsequently annealed for 2 h at 1100 °C.

The increase in melt nitrogen and the higher annealing temperature (1100 °C) achieved all three key strategies. Cr_2N particles (~15 vol%) were introduced, bringing the combined hard phase ($M_{23}C_6 + Cr_2N$) volume fraction to ~50 vol%. Nitromaxx maintained flow strength and strain-hardening levels, independent of temperature, over the range 150 to 350 °C. In contrast, the strength of the reference stainless steel

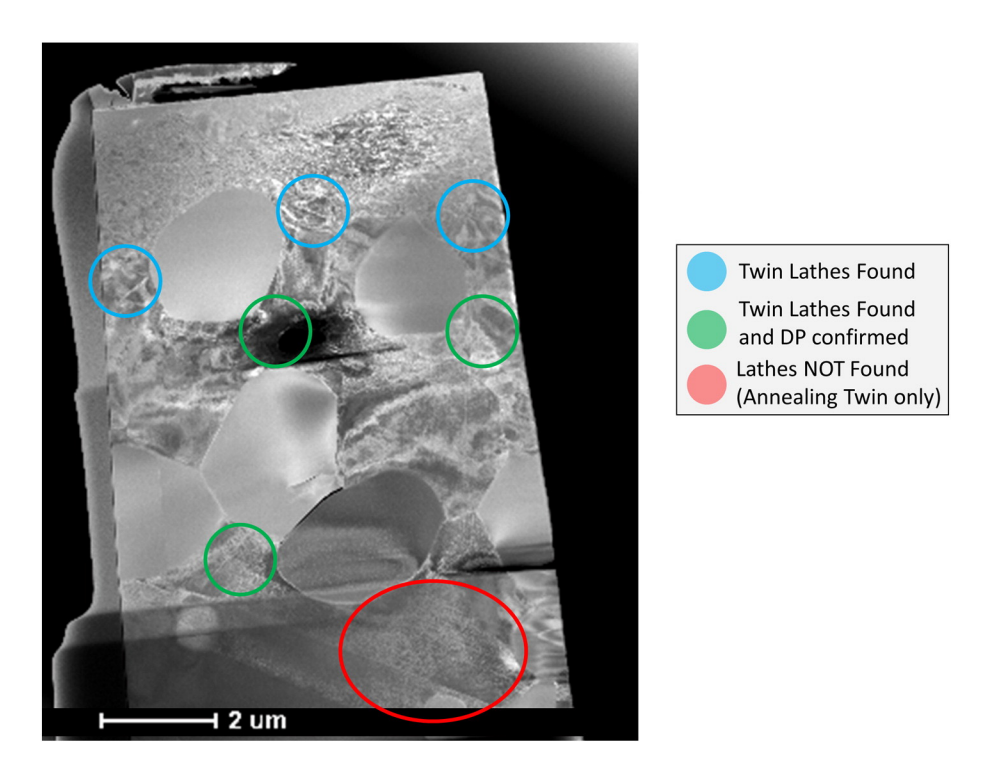


Fig. 12. Cross-section of a Nitromaxx/1100 sample, after ASTM G98 testing at 343 °C. The TEM foil shows the wear surface at the top, where the opposing surface slid out of the page. The smaller blue and green regions closer to the wear surface show where twin laths were observed.

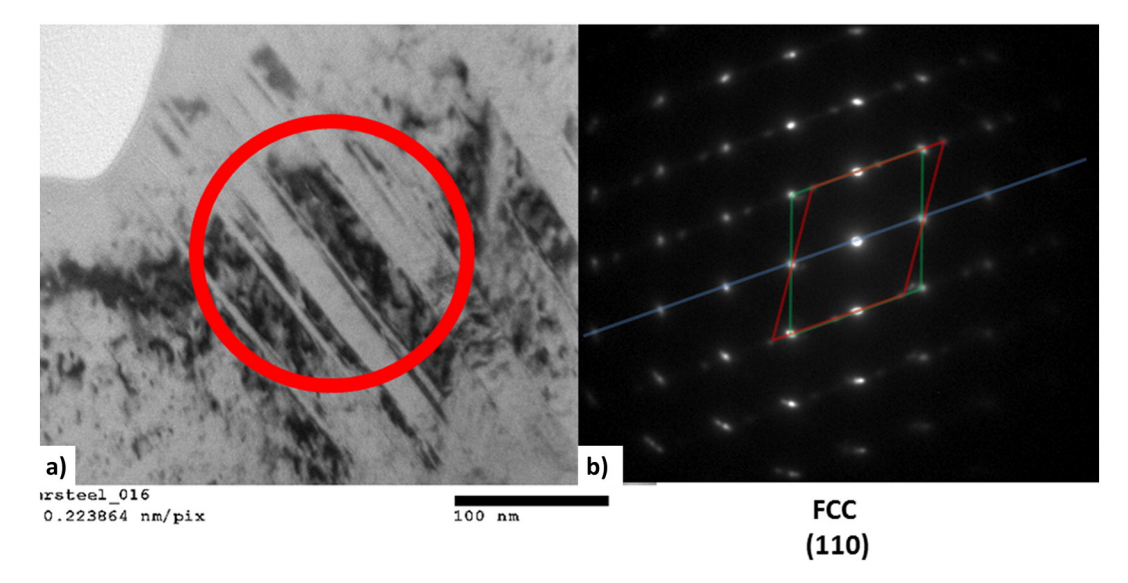


Fig. 13. (a) Morphology and structure showing the presence of deformation twins in Nitromaxx/1100 after ASTM G98 testing at 343 °C; (b) selected area diffraction patterns from regions with laths confirming twinning orientations near the wear surface (see Fig. 12). The invariant plane and twin variant spots are highlighted for clarity.

alloy, NOREM 02, which had a melt composition of ~0.17 wt% N and was annealed at 1050 °C, decreased in this regime and showed poor galling performance. An increase in melt nitrogen and a lower annealing temperature (1050 °C) achieved strategy (1) but not strategies (2) and (3) and was judged to be unsuccessful. Thus, the use of hard particles alone was judged to be insufficient to achieve high galling resistance from room temperature to 350 °C and that modification of the matrix nitrogen content was judged to be essential.

The signature constant flow strength of Nitromaxx in the 150 to 350 °C regime is correlated with deformation twinning that was observed near the worn surface of Nitromaxx but not NOREM 02 samples tested at 343 °C. The higher annealing temperature (1100 °C) for Nitromaxx was predicted by CALPHAD to increase interstitial nitrogen in the matrix. Experiments confirmed that Nitromaxx with an 1100 °C anneal exhibited a larger matrix lattice parameter, reduced stacking fault energy, enhanced strain-induced martensitic transformation at room temperature, and enhanced strain-induced twinning at elevated temperature (343 °C). The resulting Nitromaxx alloy (with ~0.5 wt% N vs. < ~0.2 wt% N for 304LN and Nitronic alloys) exhibited extraordinary galling resistance from RT to 350 °C, competitive with existing Co-base Stellite. This has particularly positive ramifications for mitigating occupational radiation exposure in nuclear power plants caused by radioactive Co.

Table 5 Stacking Fault Width d_{eff} and Stacking Fault Energy (SFE) After G98 Testing at 625 K (343 °C).

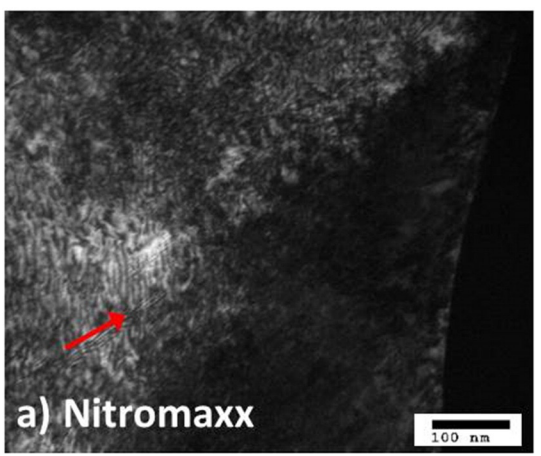
	$d_{\mathrm{eff}}\left(\mathrm{nm}\right)$	SFE (mJ/m^2) Eq. (1)
NOREM 02/1050 Nitromaxx/1100	$\begin{array}{c} 8\pm 6 \\ 14\pm 5 \end{array}$	$30 \pm 20 \\ 10 \pm 20$

Acknowledgements

This work was supported by the Electric Power Research Institute (Grant EP-P39772/C17655). Bud Labs is acknowledged for conducting the ASTM G98 testing. The authors appreciate the use of the LNNano XTMS Beamline at the LNLS in Campinas, Brazil for the in-situ XRD testing.

References

- [1] R.G. Bayer, Mechanical Wear Prediction and Prevention, Marcel Dekker, Inc., New York, NY (USA), 1994https://doi.org/10.1111/j.1475-1305.1995.tb00971.x.
- [2] B. Bhushan, Modern Tribology Handbook, CRC Press, Boca Raton, FL (USA), 2000, ISBN 9780849384035.
- [3] M.O. Speidel, Nitrogen containing austenitic stainless steels, Mater. Werkst. 37 (2006) 875–880, https://doi.org/10.1002/mawe.200600068.



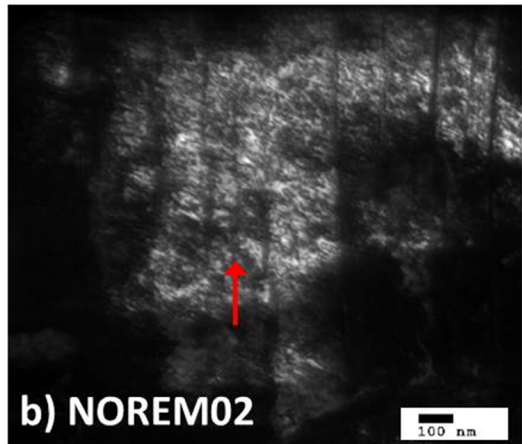


Fig. 14. Transmission Electron Microscope (TEM) images of stacking faults in stainless-steel hardfacing alloys, using weak beam dark field conditions, for (a) Nitromaxx/1100 and (b) NOREM 02/1050.

- [4] W. Wang, W. Yan, K. Yang, Y. Shan, Z. Jiang, Temperature dependence of tensile behaviors of nitrogen-alloyed austenitic stainless steels, J. Mater. Eng. Perform. 19 (2010) 1214–1219, https://doi.org/10.1007/s11665-010-9603-7.
- [5] Suzuki K. Yonezawa, S. Ooki, A. Hashimoto, The effect of chemical composition and heat treatment conditions on stacking fault energy for Fe-Cr-Ni austenitic stainless steel, Metall. Mater. Trans. A 44 (2013) 5884–5896, https://doi.org/10.1007/ s11661-013-1943-0
- [6] A. Das, Revisiting stacking fault energy of steels, Metall. Mater. Trans. A 47A (2016) 748–768, https://doi.org/10.1007/s11661-015-3266-9.
- [7] G.V. Prasad Reddy, R. Sandhya, S. Sankaran, P. Parameswaran, K. Laha, Creep-fatigue interaction behavior of 316LN austenitic stainless steel with varying nitrogen content, Mater. Des. 88 (2015) 972–982, https://doi.org/10.1016/j.matdes.2015.09. 0070264-1275.
- [8] G.B. Olson, M. Cohen, Kinetics of strain-induced martensite nucleation, Metall. Trans. A. 6A (1975) 791–795, https://doi.org/10.1007/BF02672301.
- [9] R. Zaera, J.A. Rodríguez-Martínez, A. Casado, J. Fernández-Sáez, A. Rusinek, R. Pesci, A constitutive model for analyzing martensite formation in austenitic steels deforming at high strain rates, Int. J. Plast. 29 (2012) 77–101, https://doi.org/10.1016/j.iiplas.2011.08.003.
- [10] A. Kermanpur, P. Behjati, J. Han, A. Najafizadeh, Y.K. Lee, A microstructural investigation on deformation mechanisms of Fe–18Cr–12Mn–0.05C metastable austenitic steels containing different amounts of nitrogen, Mater. Des. 82 (2015) 273–280, https://doi.org/10.1016/j.matdes.2015.05.075.
- [11] Y.B. Das, A.N. Forsey, T.H. Simm, K.M. Perkins, M.E. Fitzpatrick, S. Gungor, R.J. Moat, In situ observation of strain and phase transformation in plastically deformed 301 austenitic stainless steel, Mater. Des. 112 (2016) 107–116, https://doi.org/10. 1016/j.matdes.2016.09.057.
- [12] F.Y. Dong, P. Zhang, J.C. Pang, Y.B. Ren, K. Yang, Z.F. Zhang, Strength, damage and fracture behaviors of high-nitrogen austenitic stainless steel processed by high-pressure torsion, Scr. Mater. 96 (2015) 5–8, https://doi.org/10.1016/j.scriptamat.2014.09.016.
- [13] H.W. Lee, J.H. Kong, D.J. Lee, H.Y. On, J.H. Sung, A study on high temperature gas nitriding and tempering heat treatment in 17Cr–1Ni–0.5C, Mater. Des. 30 (2009) 1691–1696, https://doi.org/10.1016/j.matdes.2008.07.023.
- [14] K.G. Budinski, M.K. Budinski, M.S. Kohler, A galling-resistant substitute for silicon nickel, Wear 255 (2003) 489–497, https://doi.org/10.1016/S0043-1648(03)00047-4.
- [15] B. Clausen, D.W. Brown, J.S. Carpenter, K.D. Clarke, A.J. Clarke, S.C. Vogel, J.D. Bernardin, D. Spernjak, J.M. Thompson, Deformation behavior of additively manufactured GP1 stainless steel, Mater. Sci. Eng. A 696 (2017) 331–340, https://doi.org/10.1016/j.msea.2017.04.081.
- [16] A. Wang, T.A. Palmer, A.M. Beese, Effect of processing parameters on microstructure and tensile properties of austenitic stainless steel 304L made by directed energy deposition additive manufacturing, Acta Mater. 110 (2016) 226–235, https://doi.org/ 10.1016/j.actamat.2016.03.019.
- [17] B. Bhushan, Introduction to Tribology, 2nd ed. John Wiley & Sons, Hoboken, NJ (USA), 2013, ISBN 978-1-119-94453-9.
- [18] R. Chattopadhyay, Surface Wear: Analysis, Treatment and Prevention, ASM International, Materials Park, OH (USA), 2001, ISBN 0871707020.
- [19] G.E. Dieter, Mechanical Metallurgy, 3rd ed. McGraw-Hill, Boston, MA (USA), 2013, ISBN 1259064794.
- [20] J.C. Lippold, D.J. Kotecki, Welding Metallurgy and Weldability of Stainless Steels, John Wiley and Sons, Hoboken, NJ (USA), 2005, ISBN 978-0-471-47379-4.
- [21] E. Rabinowicz, Friction and Wear of Materials, 2nd ed. John Wiley & Sons, Hoboken, NJ (USA), 2013, ISBN 978-0-471-83084-9.
- [22] J.C. Rawers, J.H. Tylczak, D.E. Alman, Wear evaluation of high interstitial stainless steels, Tribol. Trans. 51 (2008) 515–525, https://doi.org/10.1080/10402000802071285.
- P. Marshall, Austenitic Stainless Steels: Microstructure and Mechanical Properties, Elsevier Applied Science Publishers, Essex, England, 1984, ISBN 0-85334-277-6.
- [24] P.M. Anderson, J.P. Hirth, J. Lothe, Theory of Dislocations, 3rd ed. Cambridge University Press, New York, NY (USA), 2017, ISBN 0521864364.
- [25] L. Rémy, A. Pineau, Twinning and strain-induced f.c.c. h.c.p. transformation on the mechanical properties of CoNiCrMo alloys, Mater. Sci. Eng. 26 (1976) 123–132,
- https://doi.org/10.1016/0025-5416(76)90234-2.
 [26] R. Xiong, H. Peng, S. Wang, H. Si, Y. Wen, Effect of stacking fault energy on work hardening behaviors in Fe-Mn-Si-C high manganese steels by varying silicon and carbon contents, Mater. Des. 85 (2015) 707–714, https://doi.org/10.1016/j.matdes.
- [27] X.F. Fang, W. Dahl, Strain hardening and transformation mechanism of deformationinduced martensite transformation in metastable austenitic stainless steels, Mater. Sci. Eng. A 141 (1991) 189–198, https://doi.org/10.1016/0921-5093(91)90769-J.
- [28] J.W. Christian, The Theory of Transformations in Metals and Alloys, Elsevier Science, Oxford, UK, 2002, ISBN 978-0-08-044019-4.

- [29] J. Talonen, H. Hänninen, Formation of shear bands and strain-induced martensite during plastic deformation of metastable austenitic stainless steels, Acta Mater. 55 (2007) 6108–6118, https://doi.org/10.1016/j.actamat.2007.07.015.
- [30] J.H. Dumbleton, J.A. Douthett, The unlubricated adhesive wear resistance of metastable austenitic stainless steels containing silicon, Wear 42 (1977) 305–332, https:// doi.org/10.1016/0043-1648(77)90060-6.
- [31] E. Bele, V.S. Deshpande, The compressive response of idealized cermet-like materials, J. Appl. Mech. 82 (2015) 41009, https://doi.org/10.1115/1.4029782.
- [32] B. Dodd, Y. Bai, Adiabatic Shear Localization, 2nd ed. Elsevier, London, 2012, ISBN 9780080977812
- [33] T.H. Lee, C.S. Oh, S.J. Kim, S. Takaki, Deformation twinning in high-nitrogen austenitic stainless steel, Acta Mater. 55 (2007) 3649–3662, https://doi.org/10.1016/j. actamat.2007.02.023.
- [34] L. Mosecker, A. Saeed-Akbari, Nitrogen in chromium-manganese stainless steels: a review on the evaluation of stacking fault energy by computational thermodynamics, Sci. Technol. Adv. Mater. 14 (2013) 033001–033014, https://doi.org/10.1088/ 1468-6996/14/3/033001.
- [35] I.A. Yakubtsov, A. Ariapour, D.D. Perovic, Effect of nitrogen on stacking fault energy of f.c.c. iron-based alloys, Acta Mater. 47 (1999) 1271–1279, https://doi.org/10. 1016/S1359-6454(98)00419-4.
- [36] A. Kermanpur, P. Behjati, J. Han, A. Najafizadeh, Y.K. Lee, Design of a new Ni-free austenitic stainless steel with unique ultrahigh strength-high ductility synergy, Mater. Des. 82 (2015) 273–280, https://doi.org/10.1016/j.matdes.2014.06.069.
- [37] S. Curtze, V.T. Kuokkala, A. Oikari, J. Talonen, H. Hänninen, Thermodynamic modeling of the stacking fault energy of austenitic steels, Acta Mater. 59 (2011) 1068–1076, https://doi.org/10.1016/j.actamat.2010.10.037.
- [38] L. Rémy, A. Pineau, B. Thomas, Temperature dependence of stacking fault energy in close-packed metals and alloys, Mater. Sci. Eng. 36 (1978) 47–63, https://doi.org/10. 1016/0025-5416/78)90194-5.
- [39] K.J. Bhansali, A.E. Miller, The role of stacking fault energy on galling and wear behavior, Wear 75 (1982) 241–252, https://doi.org/10.1016/0043-1648(82)90151-X.
- [40] L.G. Korshunov, Y.N. Goikhenberg, N.K. Chernenko, Effect of alloying and heat treatment on the structure and tribological properties of nitrogen-bearing stainless austenitic steels under abrasive and adhesive wear, Met. Sci. Heat Treat. 49 (2007) 217–226.
- [41] J.-K. Kim, S.-J. Kim, The temperature dependence of the wear resistance of iron-base NOREM 02 hardfacing alloy, Wear 237 (2000) 217–222, https://doi.org/10.1016/ S0043-1648(99)00326-9.
- [42] R.T. Smith, T. Lolla, D. Gandy, L. Wu, G. Faria, A.J. Ramirez, S.S. Babu, P.M. Anderson, In situ X-ray diffraction analysis of strain-induced transformations in Fe- and Cobase hardfacing alloys, Scr. Mater. 98 (2015) 60–63, https://doi.org/10.1016/j. scriptamat.2014.11.003.
- [43] J. Talonen, Effect of Strain-induced Alpha'-martensite Transformation on Mechancial Properties of Metastable Austenitic Stainless SteelsPhD Dissertation Helsinki University of Technology, Helsinki, 2007 127.
- [44] T. Helander, J.O. Andersson, L. Höglund, P.F. Shi, B. Sundman, Thermo-Calc & DICTRA, computational tools for materials, Calphad 26 (2002) 273–312, https://doi.org/10.1016/S0364-5916(02)00037-8.
- [45] V.G. Gavriljuk, Nitrogen in iron and steel, ISIJ Int. 36 (1996) 738–745, https://doi. org/10.2355/isijinternational.36.738.
- [46] D. Manova, J. Lutz, J.W. Gerlach, H. Neumann, S. Mändl, Relation between lattice expansion and nitrogen content in expanded phase in austenitic stainless steel and CoCr alloys, Surf. Coat. Technol. 205 (Suppl. 2) (2011) S290–S293, https://doi.org/10.1016/j.surf.coat.2010.12.046.
- [47] V.G. Gavriljuk, H. Berns, High Nitrogen Steels: Structure, Properties, Manufacture, Applications, Springer Science & Business Media, Berlin, Germany, 1999https://doi. org/10.1007/978-3-662-03760-7.
- [48] P.M. Ahmedabadi, V. Kain, A. Agrawal, Modeling kinetics of strain-induced martensite transformation during plastic deformation of austenitic stainless steel, Mater. Des. 109 (2016) 466–475, https://doi.org/10.1016/j.matdes.2016.07.106.
- [49] M. Michiuchi, H. Kokawa, Z.J. Wang, Y.S. Sato, K. Sakai, Twin-induced grain boundary engineering for 316 austenitic stainless steel, Acta Mater. 54 (2006) 5179–5184.
- [50] E. Aerts, P. Delavignette, R. Siems, S. Amelinckx, Stacking fault energy in silicon, J. Appl. Phys. 33 (1962) 3078–3080, https://doi.org/10.1063/1.1728570.
- [51] R.E. Schramm, R.P. Reed, Stacking fault energies of seven commercial austenitic stainless steels, Metall. Trans. A. 6 (1975) 1345–1351, https://doi.org/10.1007/ BF02641927.
- [52] D.T. Pierce, J.A. Jiménez, J. Bentley, D. Raabe, D. Oskay, J.E. Wittig, The influence of manganese content on the stacking fault and austenitic/e-martensite interfacial energies in Fe-Mn-(Al-Si) steels investigated by experiment and theory, Acta Mater. 68 (2014) 238–253, https://doi.org/10.1016/j.actamat.2014.01.001.